Supporting Information

Insights into the Oxygen Vacancy Filling Mechanism in CuO/CeO_2 Catalysts: A Key Step Towards High Selectivity in Preferential CO Oxidation

Arantxa Davó-Quiñonero[a,b], Esther Bailón-García[a], Sergio López-Rodríguez[a], Jerónimo Juan-Juan[c], Dolores Lozano-Castelló[a], Max García-Melchor[b], Facundo C. Herrera[d,e], Eric Pellegrin[d,†], Carlos Escudero[d] and Agustín Bueno-López[a*]*

[a]Departamento de Química Inorgánica, Universidad de Alicante, Carretera San Vicente del Raspeig s/n E-03080, Alicante, Spain.

[b]School of Chemistry, CRANN and AMBER Research Centres, Trinity College Dublin, College Green, Dublin 2, Dublin, Ireland.

[c]Servicios Técnicos de Investigación, Universidad de Alicante, Carretera San Vicente del Raspeig s/n E-03080, Alicante, Spain.

[d]ALBA Synchrotron Light Source, Carrer de la Llum 2-26, 08290 Cerdanyola del Vallès, Barcelona, Spain

[e]Instituto de Investigaciones Fisicoquímicas Teóricas y Aplicadas (INIFTA, CONICET), Departamento de Química, Facultad de Ciencias Exactas, Universidad Nacional de La Plata, Diagonal 113 y 64, 1900 La Plata, Argentina.

[†]Current address: Carl Zeiss SMT GmbH, Rudolf-Eber-Straße. 2, 73447 Ober-kochen, Germany.

E-mail: arantxa.davo@ua.es; agus@ua.es. *Corresponding authors.

Table of content

Catalyst characterization

N_2 adsorption isotherms at –196ºC

N_2 adsorption–desorption isotherms were obtained in an automatic volumetric system (Autosorb-6, Quantachrome) after outgassing the samples at 150 ºC for 4 hours.

N_2 isotherms are shown in Figure S1, and both CeO_2 and CuO/CeO_2 present a type-IV isotherm, which is a typical feature from mesoporous materials.[1] Moreover, H2(b) hysteresis loop caused by capillary condensation phenomena evidences broad pore size distribution,[2] as expected when following the simple nitrate calcination preparation procedure. On the other hand, the lack of a plateau in the last points of adsorption branch also proves the presence of macroporosity. Comparing between CeO_2 and CuO/CeO_2 samples, the presence of CuO produces a lowering in the calculated BET surface from bare CeO_2 (Table S1) in agreement with partial pore blocking upon Cu loading.[3]

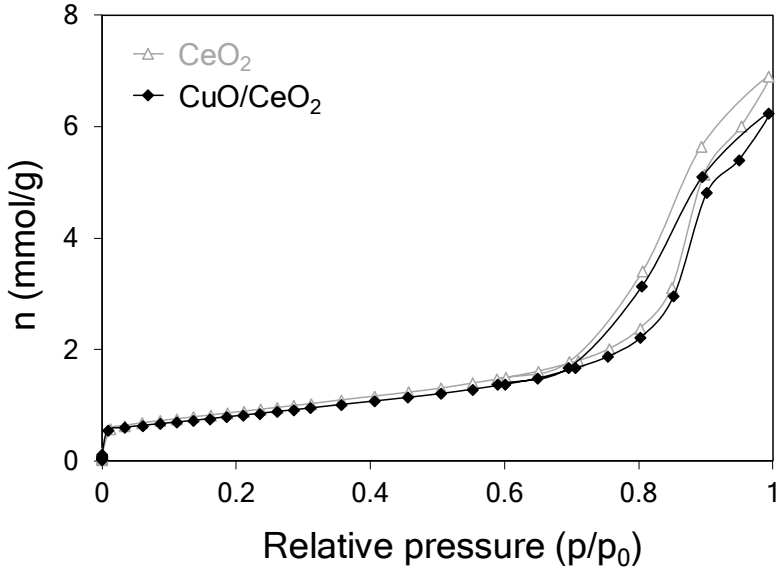

Figure S1. N_2 physisorption isotherms (–196ºC) from CeO_2 and CuO/CeO_2 samples.

Table S1. Textural results from N_2 physisorption analyses.

Sample	S_{BET} (m^2/g)	Pore V (cm^3/g)	Micro-pore $V_{(DR)}$ (cm^3/g)
CeO_2	71	0.24	0.04
CuO/CeO_2	65	0.22	0.04

X-ray Diffraction

X-ray diffractograms were recorded using Cu Kα radiation (λ=0.15418 nm) between 10 and 90º (2θ) in a Rigaku Miniflex II diffractometer. The average crystallite size of the ceria support was determined using the Scherrer[4] and Williamson-Hall's equations (WH)[5,6] and both are presented in Table S2. The crystalline distortion upon CuO loading was used to calculate the percentage of Cu inserted in CeO_2 lattice was calculated by means of the empirical equation of Kim derived from Vegard's law.[7]

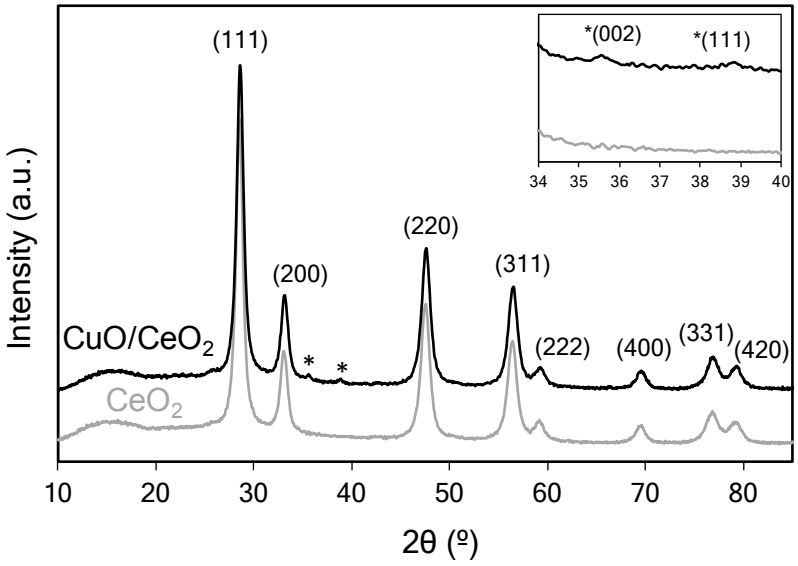

Figure S2. X-ray diffractograms recorded for CeO_2 and CuO/CeO_2 catalysts. (*) refers to CuO peaks.

Table S2. Crystallographic features of the support and catalyst.

Sample	Cell parameter (nm)	Crystallite size (nm)		% Cu in CeO_2[(a)]
		Scherrer	WH	
CeO_2	0.5420	10	13	NA
CuO/CeO_2	0.5411	10	15	0.56

[(a)]Percentage of Cu in CeO_2 solid solution calculated by Kim's equation.

The diffractograms included in Figure S2 show that both CeO_2 and CuO/CeO_2 samples display closely identical diffraction pattern, fitting with standard CeO_2 fluorite (JCPDS no. 01-075-0120). The presence of CuO is observed by the appearance of characteristic CuO tenorite tiny peaks (JCPDS no. 01-089-2529), which evidence good Cu dispersion on the CeO_2 support. On the other hand, attending to the calculated cubic cell parameter using the (111) peak, the Cu deposition leads to a lattice contraction, whereas crystallite size slightly increases. These results are in agreement with well-reported values for CeO_2-based materials[8] and allow to conclude that, though minor Cu cations insertion in the CeO_2 lattice, CuO is mainly forming a disperse segregated phase on the CeO_2 surface.

Raman spectroscopy

Raman spectra of CeO_2 and CuO/CeO_2 were recorded in a Fourier Transform Raman Spectrometer (Jasco NRS-5100) with He:Ne laser source (633 nm) and these are presented in Figure S3. The intensities have been normalized with the corresponding peak maxima of each spectrum, and since CuO/CeO_2 spectrum data had much less raw intensity, the bands appear broader than when compared to CeO_2.

The well-reported characteristic Raman spectrum for CeO_2-based oxides shows a main Raman line at 463 cm^{-1}, corresponding to the active F_{2g} mode due to the oxygen symmetric breathing vibration around Ce^{4+} ions in the bare fluorite-type CeO_2 lattice.[9] The presence of Cu in CuO/CeO_2 catalyst leads to a red shifting of the F_{2g} band to 461 cm^{-1}, which is explained by the fluorite lattice expansion upon Ce^{4+} cations reduction by the Cu^{2+}/Cu^{+}–Ce^{4+}/Ce^{3+} labile redox interaction.[10] In agreement with this, the presence of charge-compensating oxygen vacancies is evidenced by additional bands, namely the D bands positioned around 570-600 cm^{-1}.

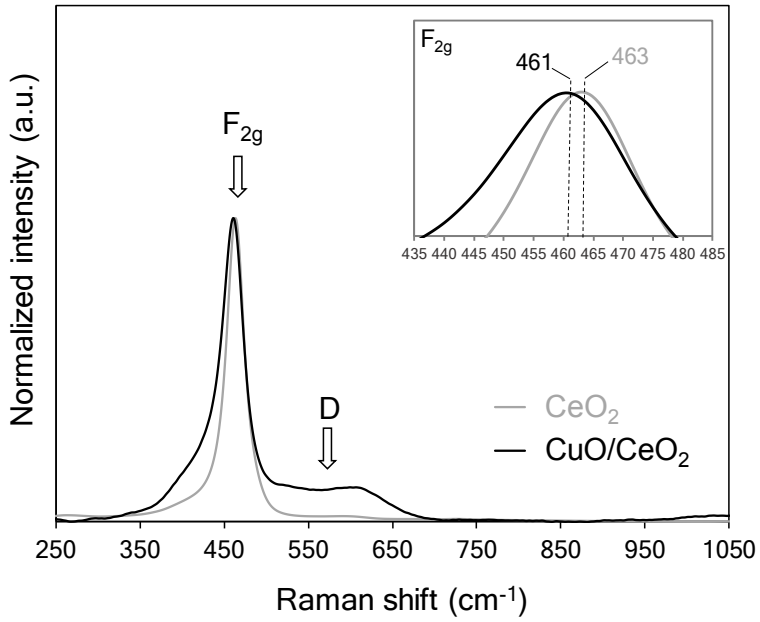

Figure S3. Raman spectra corresponding to CeO_2 and CuO/CeO_2 with main band assignations.

In summary, the presence of Cu activates surface lattice oxygen, as well as promotes the formation of defects, which leads to highly active sites with redox enhanced ability. Comparing with XRD data, since XRD and Raman spectroscopy exhibit different depth sensitivity, it can be concluded that the changes observed upon Cu loading are roughly superficial, being CuO forming segregated phase blocking CeO_2 interparticle spaces.

Temperature Programmed Reduction with H_2 (H_2-TPR)

Temperature Programmed Reduction with H_2 (H_2-TPR) experiments were conducted with 40 mg of sample in a heating ramp of 10 ºC/min up to 950 ºC in a 40 mL/min flow of 5% H_2/Ar. A CuO reference sample was used to quantify the amount of H_2 consumed in the experiments. The experiments were carried out in a Micromeritics Pulse ChemiSorb 2705 device.

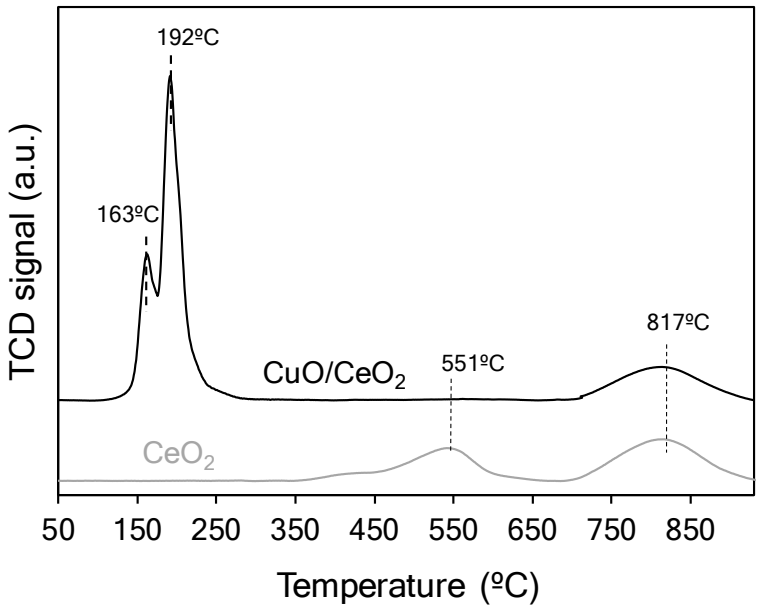

Figure S4. H_2-TPR profiles from CeO_2 and CuO/CeO_2 samples.

The reduction profiles in Figure S4 show large differences between CeO_2 and CuO/CeO_2 behavior. The well-reported H_2-TPR profile from CeO_2 displays two main regions, namely a medium temperature range at ca. 550 ºC, assigned to surface Ce^{4+} cations reduction; and a high temperature process at ca. 800 ºC, attributed to the reduction of bulk Ce^{4+} cations,[11] being in both cases Ce^{3+} the final state of cerium cations.

On the other hand, CuO/CeO_2 shows two sharp reduction peaks at low temperature, around 160 and 190 ºC, attributed to the reduction of finely disperse and large CuO particles, respectively,[12] although reduction of Cu^{2+} in two consecutive steps, first to Cu^{+} and later to Cu^{0}, cannot be ruled out. It should be noticed that bare CuO sample starts reducing in the same conditions around 350 ºC, so the anticipated reduction occurring in CuO/CeO_2 catalyst must be related to the synergistic Cu–Ce interaction, promoting the reducibility of copper species. Moreover, the labile redox exchange between Cu and Ce also affects to CeO_2 surface reduction, as it is much anticipated taking place evolved under CuO reduction peaks. The calibrated areas allow to calculate the excess of H_2 consumed in the two first peaks, and thus confirm Ce^{4+} reduction together with CuO.

In conclusion with the characterization results, the deposition of 5% Cu into the CeO_2 by impregnation conduces to extraordinary redox properties and the facile creation of oxygen vacancies, which supply great catalytic activity features to the CuO/CeO_2 catalyst.

Transmission Electron Microscopy (TEM)

TEM characterization was performed using a JEOL (JEM-2010) microscope and images were captured at different magnification. *d*-planar spacing was measured using *ImageJ* software for image analysis.

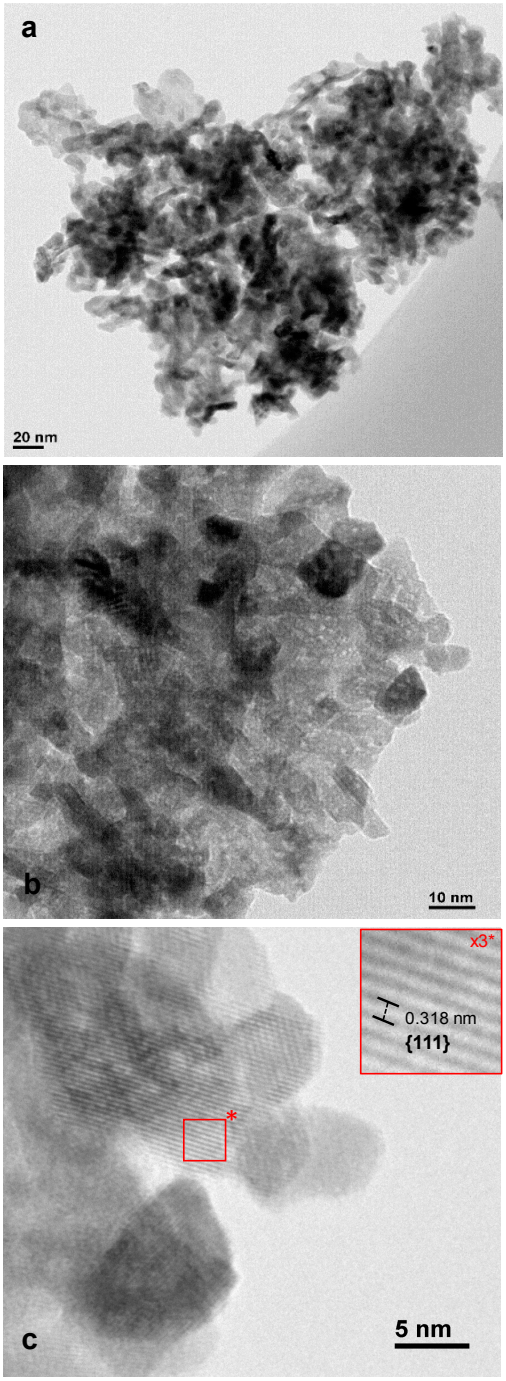

Figure S5. TEM images of CuO/CeO_2 catalyst exposing preferentially (111) planes according to *d*-spacing

CO-PROX activity tests

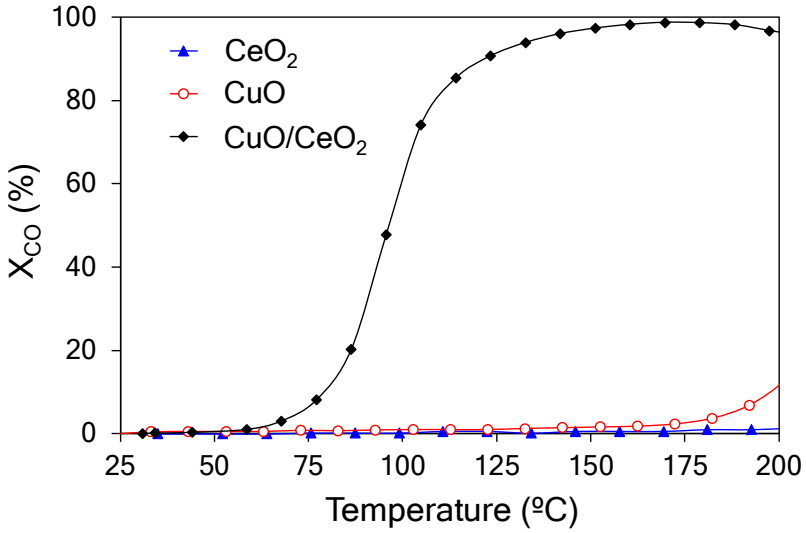

Figure S6. CO conversion (X_{CO}) profiles in CO-PROX activity tests reaction conditions with CuO/CeO_2 (diamonds), CeO_2 (triangles) and CuO (circles) fresh catalysts.

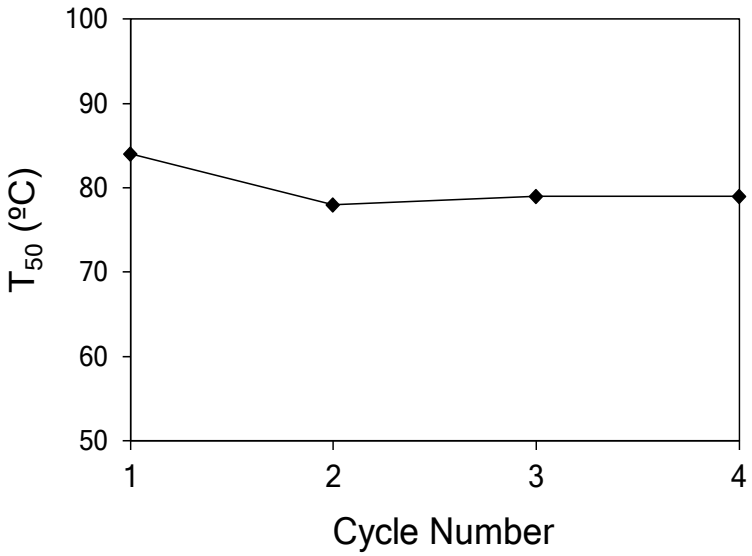

Figure S7. Temperature for the 50% of CO conversion (T_{50}) in consecutive cycles of CO-PROX activity tests with CuO/CeO_2 catalyst without pretreatment in between.

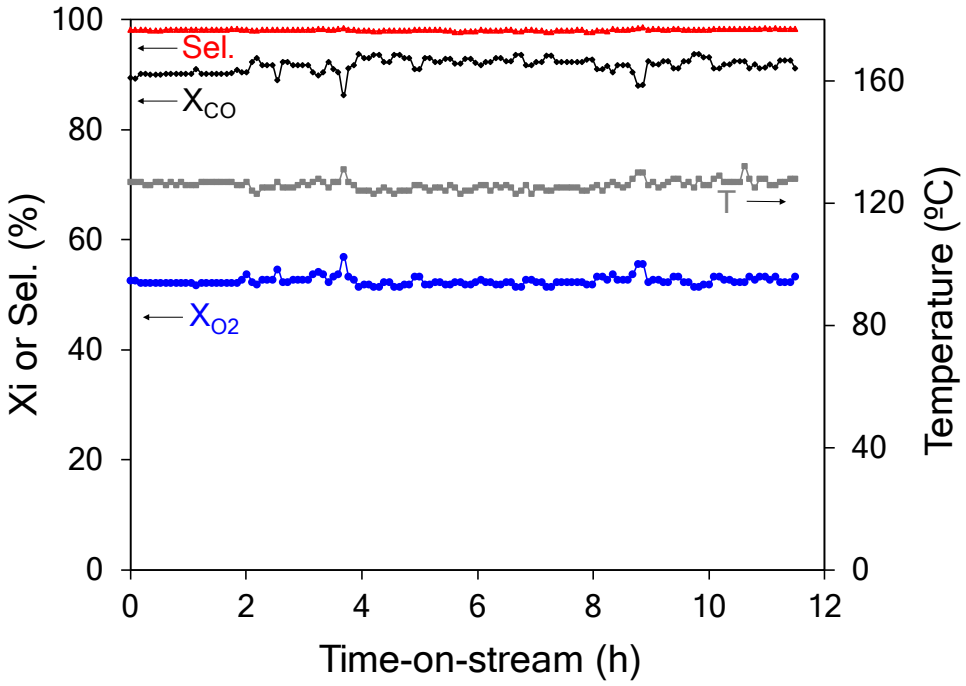

Figure S8. Catalytic performance of CuO/CeO_2 in terms of CO conversion (X_{CO}, black curve), O_2 conversion (X_{O2}, blue curve), and CO selectivity (*Sel*, red curve) in isothermal conditions during long time-on-stream CO-PROX reaction test (fifth cycle).

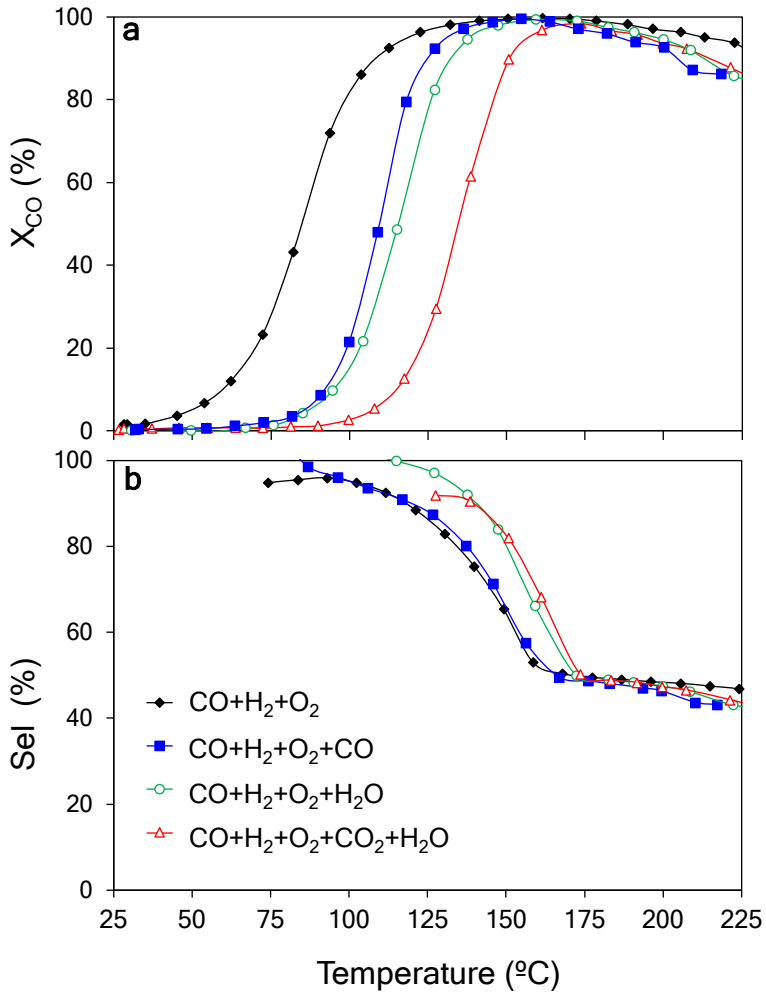

Figure S9. CO oxidation light-off curves (first run) in CO-PROX conditions in simple CO + O_2 + H_2 mixture (diamonds), the addition of 10% CO_2 (squares), 5% H_2O (circles) and 10% CO_2 + 5% H_2O (triangles). (a) CO conversion (%, X_{CO}), (b) CO selectivity (%, *Sel*).

The addition of H_2O in the reactant stream, either individually or in co-presence of CO_2 shifts the selectivity profile by the thermodynamic inhibition of H_2 oxidation reaction. The impact of H_2O in the CO oxidation catalytic activity results more detrimental than CO_2 itself. According to the reported data, while the addition of CO_2 leads to the carbonatation of ceria, H_2O shows prevalence to block Cu–O–Ce sites with a direct role in the reaction, which turns into a stronger CO oxidation inhibition.[13,14]

Temperature programmed desorption (TPD) experiments

TPD experiments were conducted using 80 mg of catalyst pretreated at 400 ºC under Ar flow (100 mL/min). Subsequently, the reactor is cooled down to 150 ºC, when the Ar atmosphere is switched to 10% CO_2 (for CO_2-TPD), 5% H_2O (for H_2O-TPD) or 10% CO_2 + 5%H_2O (for CO_2+H_2O-TPD), 100 mL/min in Ar balance. The saturation step was kept in for 1 hour in each condition and then inlet gases were switched back to Ar flow. Outlet gases were monitored with a mass spectrometer (Pfeiffer Vacuum, model OmniStar) and once CO_2 and H_2O signals were stabilized, the reactor was heated up to 650 ºC.

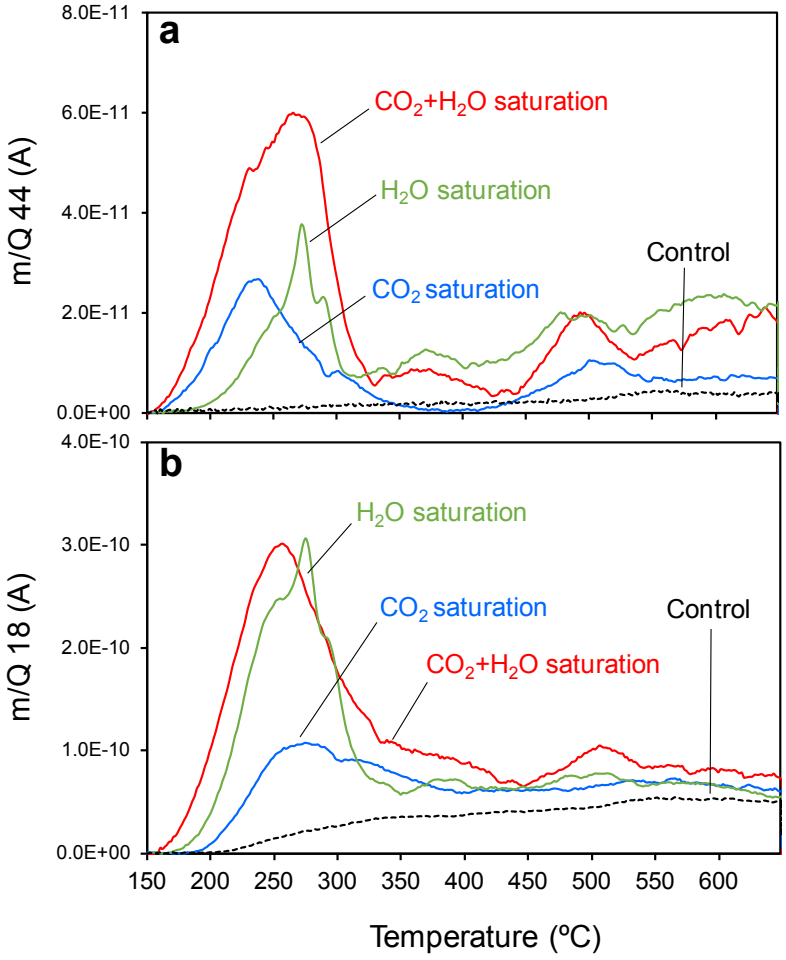

Figure S10. (a) CO_2 release, and (b) H_2O release in TPD experiments performed in Ar flow on CuO/CeO_2 catalyst after saturation with (i) CO_2, (ii) H_2O, or (iii) CO_2 + H_2O, as well as (iv) control, with no prior saturation.

Pulse isotopic experiments

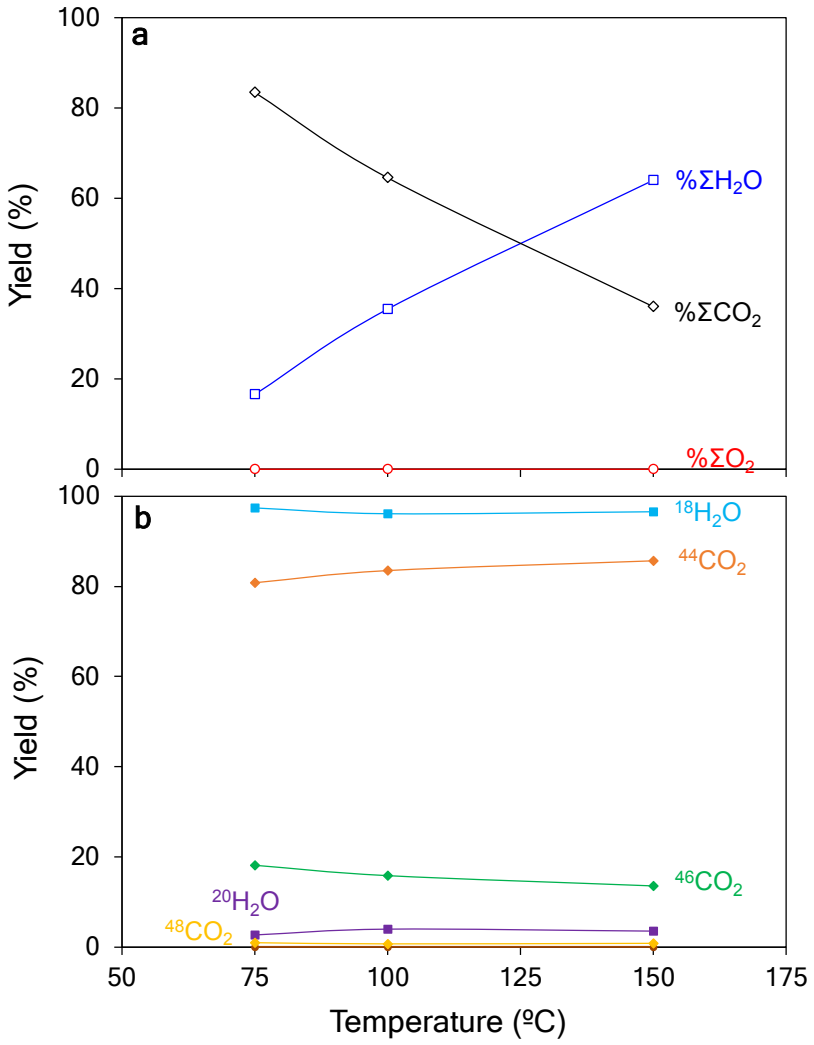

Figure S11. Product analysis after the $^{36}O_2$ pulse at different temperatures. (a) Global yield of CO_2, H_2O and O_2 species, (b) isotopic product distribution in H_2O% and CO_2% balances.

Operando CO-PROX DRIFTS–MS

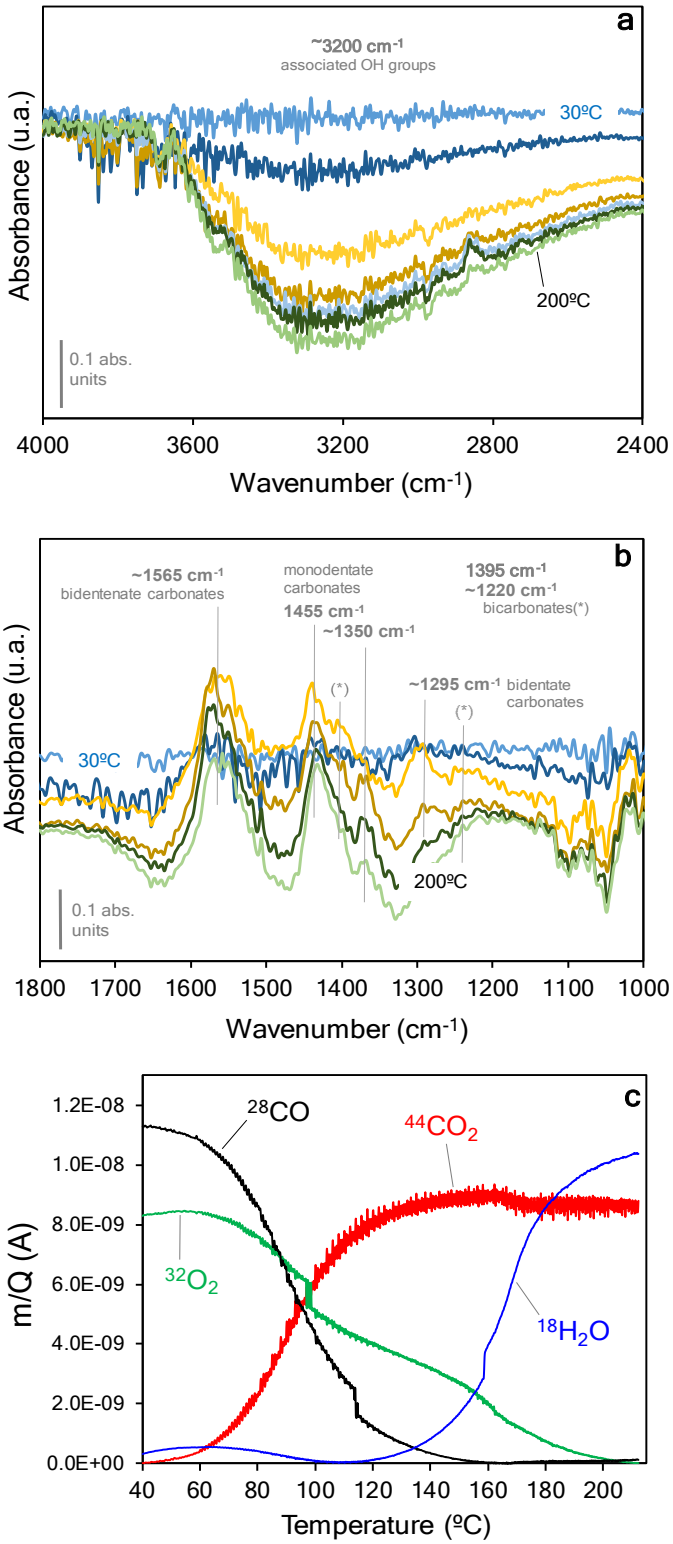

Figure S12. CO-PROX operando DRIFT spectra with CuO/CeO_2 catalyst divided in regions: (a) 2400-4000 cm^{-1}; (b) 1000-1800 cm^{-1}; (c) outlet gases evolution monitored by coupled MS.

Operando DRIFTS experiments were performed in an infrared spectrometer from Jasco (FT/IR-4000 series) using a Praying Mantis (Harrick Scientific) reaction cell with temperature and gas flow control where 120 mg of CuO/CeO_2 catalyst were placed. The chamber was purged in Ar atmosphere (50 mL/min) and a spectrum was recorded at room temperature. This Ar-background spectrum will be subtracted from each spectrum in order to assess the evolution of surface species created and depleted by the effect of the interacting atmosphere. Subsequently, the CO-PROX gas mixture (2% CO, 2% O_2, 30% H_2, 50 mL/min balance Ar was introduced in the DRIFTS chamber by means of mass flow controllers (Bronkhorst) and spectra (900-4000 cm^{-1}) were recorded at different temperatures once stationary state was reached in each point. Product gas evolution was monitored with a spectrometer (MS) Pfeiffer Vacuum OmniStar coupled to the outlet of DRIFT chamber.

CO-PROX operando NAP–XPS experiments

Table S3. Estimated analytical surface depths (in Å) for copper and cerium oxides and for the photon energies used in this study in the NAP–XPS experiments.[18-20]

	1372 eV	**1082 eV**
Ce_2O_3	22.3	18.6
CeO_2	21.8	18.2
CuO	23.9	19.9

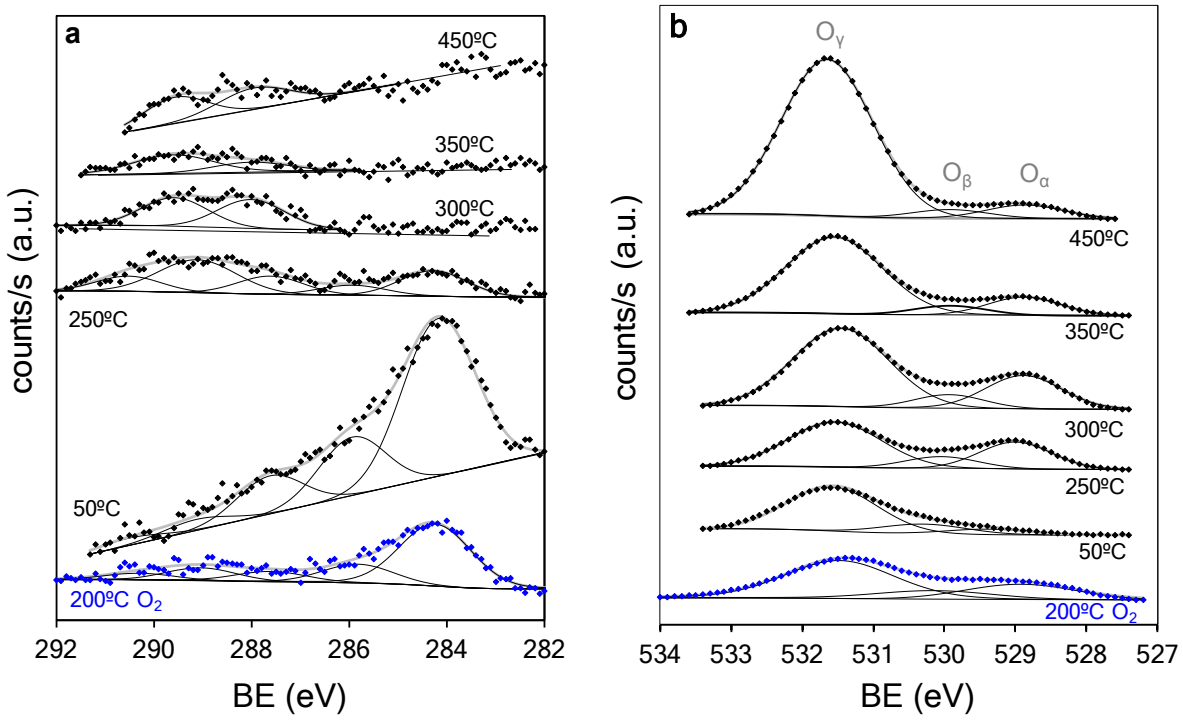

Figure S13. (a) C 1s and (b) O 1s XPS region analyses of the CuO/CeO_2 catalyst in O_2 (blue) and CO-PROX reaction conditions (black) at different temperatures taken at 722 eV photon energy.

DFT calculations

Table S4. O vacancy formation energies ($E_{O\text{-}vac}$, in eV) according to different localization of the excess of electrons for the $CeO_2(111)$, CuO(111) and $Cu_2O(111)$ surface slabs. *NN* and *NNN* refer to nearest neighbour and next nearest neighbour, respectively.

	$CeO_2(111)$		CuO(111)	$Cu_2O(111)$
e^- localization	*NN* / *NNN*	*NN* / *NN*	*NN* / 2*(*NN*/2)	delocalized
$E_{O\text{-}vac}$	2.22	2.42	2.34	1.95

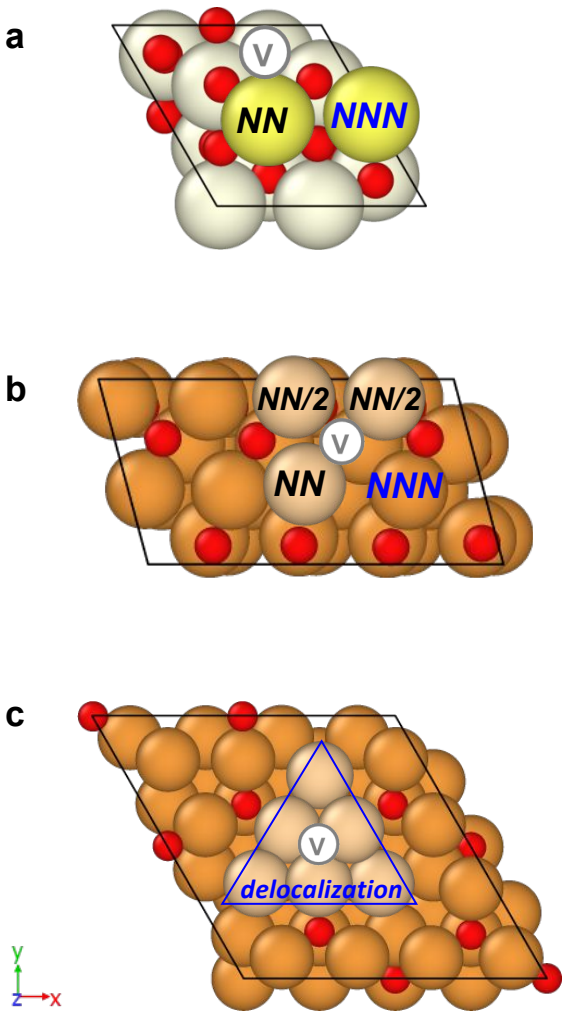

Figure S14. Top views of the DFT-modelled surface slabs with 1 O surface vacancy: a) CeO_2(111), Ce in light yellow and O in red; b) CuO(111) and c) Cu_2O(111), Cu in brown. *V* marks the location of the oxygen vacancy and *NN*, *NNN* the position of the nearest neighbor and next nearest neighbor to the O vacancy, respectively. Shaded ions show reduced cations in the best rearrangement.

Supporting References

(1) Lowell, M.; Shields, S.; Thomas, J.E.;Thommes, M.A. *Characterization of Porous Solids and Powders: Surface Area, Pore Size and Density*, 1st Edition; Particle Technology Series (1567-827X); Springer Netherlands: Heidelberg, 2004.

(2) Thommes, M.; Kaneko, K.; Neimark, A.V.; Olivier, J.P.; Rodríguez-Reinoso, F.; Rouquerol, J.; Sing, K.S.W. Physisorption of gases, with special reference to the evaluation of surface area and pore size distribution (IUPAC Technical Report). *Pure Appl. Chem.* **2015,** *87*, 1051–1069.

(3) Brunauer, S.; Emmett, P.H.; Teller, E.; Adsorption of Gases in Multimolecular Layers. *J. Am. Chem. Soc.* **1938,** *60*, 309–319.

(4) Scherrer, P. Bestimmung der Größe und der inneren Struktur von Kolloidteilchen mittels Röntgenstrahlen, *Nachr. Ges. Wiss. Göttingen*, **1918,** *26*, 98–100.

(5) Williamson, G.K.; Hall, W.H. X-ray line broadening from filed aluminium and wolfram. *Acta Metall.* **1953,** *1*, 22–31.

(6) Burton, A.W.; Ong, K.; Rea, T.; Chan, I.Y. On the estimation of average crystallite size of zeolites from the Scherrer equation: A critical evaluation of its application to zeolites with one-dimensional pore systems. *Microporous Mesoporous Mater.* **2009,** *117*, 75–90.

(7) Kim, D.J. Lattice Parameters, Ionic Conductivities, and Solubility Limits in Fluorite-Structure MO_2 Oxide (M = Hf^{4+}, Zr^{4+}, Ce^{4+}, Th^{4+}, U^{4+}) Solid Solutions. *J. Am. Ceram. Soc.* **1989,** *72*, 1415–1421.

(8) Aneggi, E.; Wiater, D.; de Leitenburg, C.; Llorca, J.; Trovarelli, A. Shape-Dependent Activity of Ceria in Soot Combustion. *ACS Catal.* **2014,** *4*, 172–181.

(9) Trovarelli, A. Catalytic Properties of Ceria and CeO_2-Containing Materials. *Catal. Rev.* **1996,** *38*, 439–520.

(10) Avgouropoulos, G.; T. Ioannides, T.; Matralis, H. Influence of the preparation method on the performance of CuO–CeO_2 catalysts for the selective oxidation of CO. *Appl. Catal., B* **2005,** *56,* 87–93.

(11) Johnson, M.F.L.; Mooi, J. Cerium dioxide crystallite sizes by temperature-programmed reduction. *J. Catal.* **1987,** *103*, 502–503.

(12) Martínez-Arias, A.; Gamarra, D.; Hungría, A.; Fernández-García, M.; Munuera, G.; Hornés, A.; Bera, P.; Conesa, J.; Cámara, A. Characterization of Active Sites/Entities and Redox/Catalytic Correlations in Copper-Ceria-Based Catalysts for Preferential Oxidation of CO in H_2-Rich Streams. *Catalysts* **2013,** *3*, 378–400.

(13) Gamarra, D.; Martínez-Arias, A. Preferential oxidation of CO in rich H_2 over CuO/CeO_2: Operando-DRIFTS analysis of deactivating effect of CO_2 and H_2O. *J. Catal.* **2009,** *263*, 189–195.

(14) Lee, H.; Kim, D. Kinetics of CO and H_2 oxidation over $CuO\text{-}CeO_2$ catalyst in H_2 mixtures with CO_2 and H_2O. *Catal. Today* **2008,** *132*, 109–116.

.